ARL-TR-9289 ● SEP 2021

DEVCOM ARMY RESEARCH LABORATORY

Imidazolium Perchlorate: A Novel Energetic Molecular Ferroelectric

by Jennifer L Gottfried, Chi-Chin Wu, Rose A Pesce-Rodriguez, Scott D Walck, and Shenqiang Ren

NOTICES

Disclaimers

The findings in this report are not to be construed as an official Department of the Army position unless so designated by other authorized documents.

Citation of manufacturer's or trade names does not constitute an official endorsement or approval of the use thereof.

Destroy this report when it is no longer needed. Do not return it to the originator.

ARL-TR-9289 ● SEP 2021

Imidazolium Perchlorate: A Novel Energetic Molecular Ferroelectric

Jennifer L Gottfried, Chi-Chin Wu, and Rose A Pesce-Rodriguez
Weapons and Materials Research Directorate,
DEVCOM Army Research Laboratory

Scott D Walck
SURVICE Engineering Company

Shenqiang Ren
The State University of New York–Buffalo

REPORT DOCUMENTATION PAGE

Form Approved
OMB No. 0704-0188

1. REPORT DATE *(DD-MM-YYYY)*	2. REPORT TYPE	3. DATES COVERED (From - To)
September 2021	Technical Report	October 2020–June 2021

4. TITLE AND SUBTITLE
Imidazolium Perchlorate: A Novel Energetic Molecular Ferroelectric

5a. CONTRACT NUMBER

5b. GRANT NUMBER

5c. PROGRAM ELEMENT NUMBER

6. AUTHOR(S)
Jennifer L Gottfried, Chi-Chin Wu, Rose A Pesce-Rodriguez, Scott D. Walck, and Shenqiang Ren

5d. PROJECT NUMBER

5e. TASK NUMBER

5f. WORK UNIT NUMBER

7. PERFORMING ORGANIZATION NAME(S) AND ADDRESS(ES)
DEVCOM Army Research Laboratory
ATTN: FCDD-RLW-WA
Aberdeen Proving Ground, MD 21005

8. PERFORMING ORGANIZATION REPORT NUMBER
ARL-TR-9289

9. SPONSORING/MONITORING AGENCY NAME(S) AND ADDRESS(ES)

10. SPONSOR/MONITOR'S ACRONYM(S)

11. SPONSOR/MONITOR'S REPORT NUMBER(S)

12. DISTRIBUTION/AVAILABILITY STATEMENT
Approved for public release: distribution unlimited.

13. SUPPLEMENTARY NOTES
ORCID IDs: Jennifer Gottfried, 0000-0002-1282-1928; Chi-Chin Wu, 0000-0002-6036-3271; Shenqiang Ren, 0000-0002-9987-3316

14. ABSTRACT
We have investigated the changes in structure, composition, and microsecond-timescale energy release behavior for a molecular ferroelectric salt, imidazolium perchlorate ($ImClO_4$), as a function of polarization. Low-temperature heating sufficient to depolarize the $ImClO_4$ results in desorption of imidazole rings and significant morphological changes at the atomic scale but does not influence the microsecond-timescale energy release. Higher temperature pyrolysis at 350 °C produces a large exotherm and gas-combustion products such as H_2O, CO/N_2, and CO_2. The estimated detonation velocity measured via the laser-induced air shock from energetic materials method was 7.2 km/s, which is comparable to the military explosive hexanitrostilbene. Despite its relatively unfavorable oxygen balance (–43%), the ferroelectric properties of $ImClO_4$ may make it suitable for specialized energetic applications.

15. SUBJECT TERMS
differential scanning calorimetry, DSC, electric field, energetic material, ferroelectric, fast Fourier transform, FFT, laser-induced air shock for energetic materials, LASEM, micro-electro-mechanical systems, MEMS, transmission electron microscopy, TEM, X-ray energy dispersive spectroscopy, XEDS

16. SECURITY CLASSIFICATION OF:			17. LIMITATION OF ABSTRACT	18. NUMBER OF PAGES	19a. NAME OF RESPONSIBLE PERSON
a. REPORT	b. ABSTRACT	c. THIS PAGE			Jennifer L Gottfried
Unclassified	Unclassified	Unclassified	UU	33	19b. TELEPHONE NUMBER (Include area code) (410) 278-7573

Standard Form 298 (Rev. 8/98)
Prescribed by ANSI Std. Z39.18

Contents

List of Figures

List of Tables

Acknowledgments

This work was supported by the DEVCOM Army Research Laboratory's 6.2 project "Explosives for Long Range Cooperative Engagements" under the Long Range Distributive and Cooperative Engagements Essential Research Program. Shenqiang Ren acknowledges funding support on this work from US Army Research Office Award W911NF-18-2-0202. The collaboration between the State University of New York–Buffalo and DEVCOM ARL is under ARL's Cooperative R&D Agreements (CRADA-20-048-J001).

1. Introduction

In the quest to develop new capabilities to support our warfighters, the US Combat Capabilities Developmental Command Army Research Laboratory is investigating novel energetic materials for military applications. Metamaterials, composite materials that have been engineered to exhibit properties not usually found in natural materials, are of increasing interest in many fields including energetics research. A dielectric material is a material that transmits electric force without conduction (i.e., an insulator) and can therefore be polarized by an applied external electric field. Ferroelectric materials have a permanent electric dipole (i.e., spontaneous polarization) that can be reversibly changed through the application of an external voltage, mechanical impact (piezoelectric), or temperature change (pyroelectric) due to the strong intrinsic coupling between polarization and deformation. The first reported molecular ferroelectric materials were potassium sodium tartrate tetrahydrate, also known as Rochelle salt,[1,2] and potassium dihydrogenphosphate.[3] The discovery of ferroelectricity in perovskite oxides led to rapid development of the field.[4] In contrast to these heavy-metal-containing materials, organic ferroelectric materials are more flexible, lightweight, and easier to process, typically at the expense of smaller polarization and piezoelectric coefficients.[5]

Imidazolium perchlorate ($ImClO_4$) is a transparent, water-soluble, molecular ferroelectric metamaterial[5–12] suitable for spin coating[5,10] and 3D printing.[12] It also has a large electro-optic activity, which enables the transmittance to be varied by linear electro-optic, piezoelectric, and interference effects.[10] The trigonal $ImClO_4$ crystals consist of hexagonal-type domains and are connected by hydrogen bonding; a variety of external stimuli can be applied to reversibly change the refractive index of the individual domains. $ImClO_4$ has high spontaneous polarization, a high Curie temperature, a low coercive field (i.e., the strength of the electric field at which the macroscopic polarization of the ferroelectric capacitor disappears),[5] and a large pyroelectric coefficient (–6,334 μC m^{-2} K^{-1}) enabling high specific power.[13] The Curie temperature (T_C), or Curie point, is the temperature above which a material undergoes a phase transition from ferroelectric to paraelectric (i.e., dipole re-alignment leads to a complete loss of polarization). When heated above T_C, the crystals will lose polarization. For $ImClO_4$, T_C = 373.6 K (100.5 °C), and the spontaneous polarization reaches 9.3 μC cm^{-2} at 310 K, one of the highest among molecular ferroelectrics.[10] The properties of $ImClO_4$ are summarized in Fig. 1.

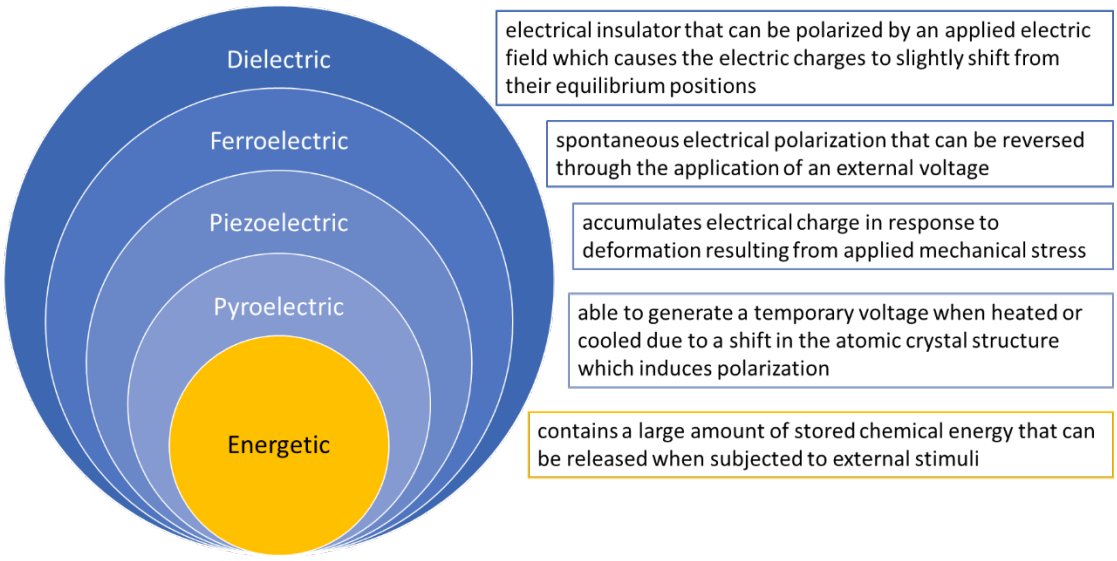

Fig. 1 Selected properties of $ImClO_4$ crystals distinguishing them from other dielectric materials.

In addition to its ferroelectric properties, both the ionic imidazolium[14–18] and perchlorate[14,19–26] components of the $ImClO_4$ salt (Fig. 2) are of interest in modern energetic material formulations. With the molecular formula $C_3H_5ClN_2O_4$, $ImClO_4$ has an oxygen balance of –43%. For comparison, the oxygen balance of the strong oxidizer ammonium perchlorate is +27%; the underoxidized molecular explosives hexanitrostilbene (HNS) and trinitrotoluene have oxygen balances of –68% and –74%, respectively. Of the common military molecular explosives, pentaerythritol tetranitrate (PETN) has the best oxygen balance (–10%) but is sensitive to shock and friction. Although several high-explosive crystals, including PETN, are known to be piezoelectric, only recently have systematic studies begun on how to use this effect[27] (e.g., as part of the Piezoenergetics: Coupled Piezoelectric and Nanoenergetic Materials with Adaptable and Tailorable Reactivity multi-university research initiative funded by the US Air Force Office of Scientific Research. In addition to the common applications for ferroelectric materials such as sensing, actuation, data storage, electro-optics, and molecular/flexible electronics, potential applications for $ImClO_4$ include micro-electro-mechanical system devices[28] with stored chemical energy on-chip,[29] on-demand sensitivity enhancement for smart energetics,[30] and electrical charging for explosive initiation or detonation enhancement.[31] Here, we supplement our previous work[13] investigating the energetic properties of spontaneously polarized $ImClO_4$ by comparing the properties of the polarized versus depolarized crystals.

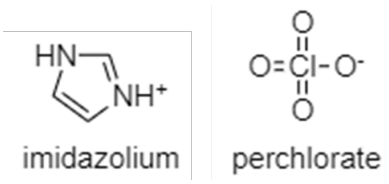

Fig. 2 Molecular structure of $ImClO_4$ salt crystals

2. Experimental

2.1 Materials

The $ImClO_4$ sample was synthesized at The State University of New York (SUNY)–Buffalo by dissolving the imidazole base in distilled water and reacting it with perchloric acid. The salt was then recrystallized from the distilled water following neutralization of the solution and sent to DEVCOM Army Research Laboratory for characterization. Confirmation of the composition of the $ImClO_4$ and ferroelectric characterization was performed at SUNY–Buffalo and detailed elsewhere.[13]

2.2 TEM

The morphology and in-depth nanoscale structural and chemical features of the as-received and heated samples were studied via transmission electron microscopy (TEM) using a JEOL JEM-2100F TEM operated at 200-keV accelerating voltage. The TEM specimens were prepared by using acetone to suspend the particles onto the holey carbon support film of TEM copper grids (300 mesh, Ted Pella, Inc) following sonication for 3 min; the thermally treated crystal was crushed between two microscope slides prior to suspension in acetone to produce particles thin enough for TEM analysis. The prepared samples were stored in a desiccator continuously purged with pure nitrogen until ready to be examined by TEM. X-ray energy dispersive spectra (XEDS) were acquired in both TEM and scanning TEM (STEM) modes to study chemical compositions in different regions. High-resolution bright field TEM (HRTEM) and high-angle annular dark-field (HAADF) images were acquired to study the details of crystalline features for as-received and heated $ImClO_4$ samples for comparison. All TEM images were analyzed ex situ using the Gatan Microscopy Suite Software (GMS, version 3.4.32, Gatan Inc) and different specific tools available in the package.

2.3 DSC/TGA

Differential scanning calorimetry (DSC) analyses were carried out using a TA Instruments (New Castle, Delaware) Q2000 instrument interfaced to a TA Instruments refrigerated cooling system (RCS90) operating under TA Universal Analysis software. Samples were heated at rate of 10 °C/min under a nitrogen flow (50 mL/min). Thermogravimetric analysis (TGA) was performed using a TA Systems Q500 TGA. Samples were run under an inert atmosphere (nitrogen flowing at 60 mL/min) at a heating rate of 10 °C/min. Depolarization of $ImClO_4$ was achieved by heating large crystals (not powder) having a total mass of approximately 8 mg to 150 °C (above T_C) and then holding at that temperature for 1 min before cooling at 200 °C/min (fastest rate allowed).

2.4 D/P–GC/MS

Desorption and pyrolysis (D/P) products were analyzed by means of a gas chromatography/mass spectrometry (GC/MS) instrument with a desorption interface. Desorption was achieved via a CDS Analytical Model 2000 Pyroprobe (coil type) connected through a heated interface chamber to the splitless injector of an Agilent (Santa Clara, California) GC/MS system (Model 6890N GC and Model 5973N MSD). The GC column used was a HP-5 capillary column (0.25 mm × 30 m, 0.25-μm film). The injector temperature was 250 °C; the Pyroprobe interface was set to a temperature of 175 °C. The GC oven temperature program was as follows: 100 °C isothermal for 1 min, 100–250 °C at 40 °C/min, and 250 °C isothermal for 1 min. The Pyroprobe was programmed to give a 20-s desorption pulse at temperatures of 175 and 350 °C at a heating rate of 1000 °C/s. The pulse temperature is based on calibration provided by the vendor and was not measured for this study. Samples (approximately 1 mg) were held within the coil of the Pyroprobe by first placing them in a quartz tube containing a small plug of glass wool, and then inserting the entire tube into the coil.

2.5 LASEM and Diagnostics

The laser-induced air shock from energetic materials (LASEM) technique was performed as previously described.[32] Samples for LASEM analysis were prepared by spreading a thin layer of several milligrams of material on a piece of double-sided tape affixed to a glass microscope slide; larger crystals were lightly crushed and pressed into the tape with a spatula prior to spreading so multiple laser shots could be acquired. Briefly, a nanosecond-pulsed laser is focused just below the sample surface to ablate micrograms of material and form a laser-induced plasma in the air above the sample, resulting in the atomization, ionization, and/or

excitation of the ablated material. Most of the energy in the laser pulse is absorb by the plasma, resulting in a heating rate on the order of 10^{13} K/s. On the microsecond timescale, high-temperature chemical reactions of the excited material occur. These reactions influence the velocity of the laser-induced shock wave generated by the focused laser pulse as it passes through the plasma region (i.e., for approximately 7–9 μs depending on the sample). Once the shock wave has expanded into the air above the reaction region, drag from the air rapidly reduces the velocity to the speed of sound in air. Measurement of the characteristic laser-induced shock velocity for a material under a given set of experimental conditions thus provides a method for comparing the energy released by the rapidly heated material on a microsecond timescale. For detonable materials, the measured laser-induced shock velocity can be directly correlated to detonation velocities obtained via large-scale detonation testing, suggesting that the laser-induced shock velocities provide a quantitative measure of the amount of material reacting exothermically on a detonation-relevant timescale.[33] For each sample, high-speed videos from 20–25 laser shots were obtained. The laser-induced plasma emission spectra were also obtained and integrated over 10 μs (delayed by 1.5 μs to minimize the broadband continuum emission from excited electrons in the plasma). Plasma emission was collected by a reflective collimator based on a parabolic mirror with a UV-enhanced Al coating and delivered to an echelle/intensified charge-coupled device detector (Catalina Scientific SE200 with an Apogee camera, 200–1000 nm, $\Delta\lambda/\lambda$=2700, gain set to 890) via a fiber optic cable.

3. Results

3.1 Structural Characterization (TEM)

The as-received $ImClO_4$ exhibits high crystallinity even in low magnifications without a significant amorphous phase, as shown in Fig. 3. In this figure, details of the crystalline features in the red bracket enclosure are further studied and shown in Fig. 3b and 3c. As exhibited in Fig. 3b, the pronounced moiré fringes appear in pairs with spacings much larger than the typical atomic arrangements in a crystal for any specific crystallographic diffraction planes. They are presumably contributed by the interactions of electron beams after going through crystalline domains of different orientations that we hypothesize to be associated with crystal polarities (Fig. 3c).

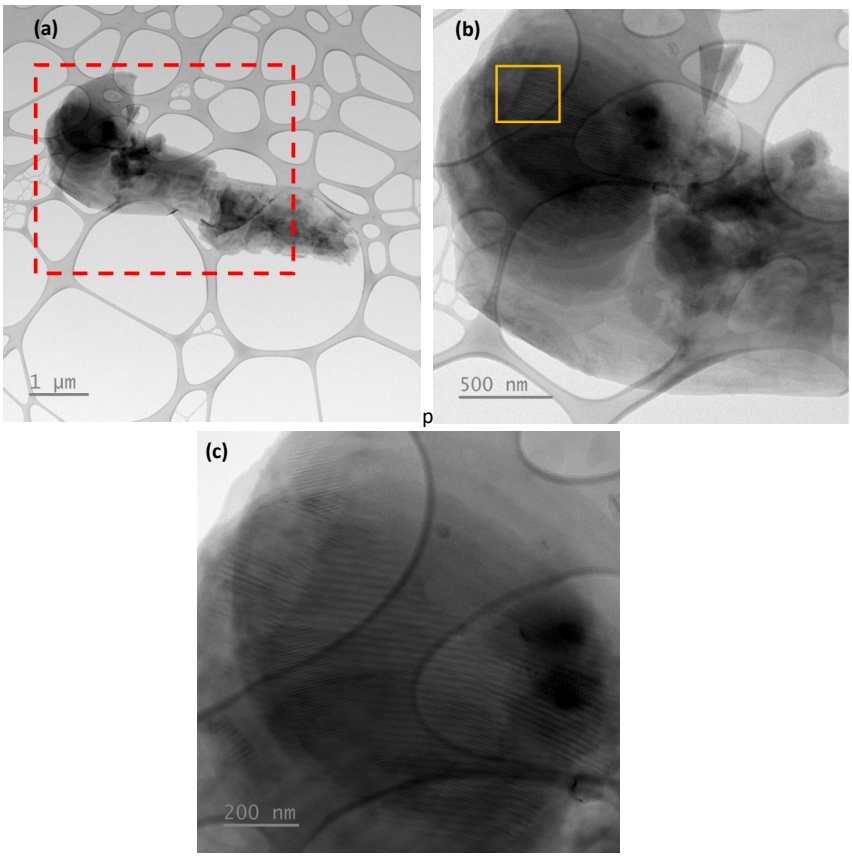

Fig. 3 TEM images of the as-received $ImClO_4$ showing (a) the highly crystalline morphology of a representative grain at a low 6,000 magnification, (b) the strong moiré fringes in the region within the dashed red bracket in (a) at 20,000 magnification, and (c) the pairwise fringes in various orientations at 40,000 magnification with the region specified by the yellow bracket in (b)

Further investigation via HRTEM shows tiny minicrystallites of only a few nanometers in size in the as-received $ImClO_4$ crystal, as indicated by the gold arrows shown in Fig. 4a. XEDS acquired in this region shows a tremendously dominant carbon (C) peak with tiny peaks showing trivial elements including a small chlorine (Cl) peak (Fig. 4b) and little or no oxygen (O)—in contrast to the surrounding region (shown in Fig. 7 and discussed later). XEDS is not sensitive to hydrogen (H); it is not clear why no nitrogen (N) from the imidazole is observed.

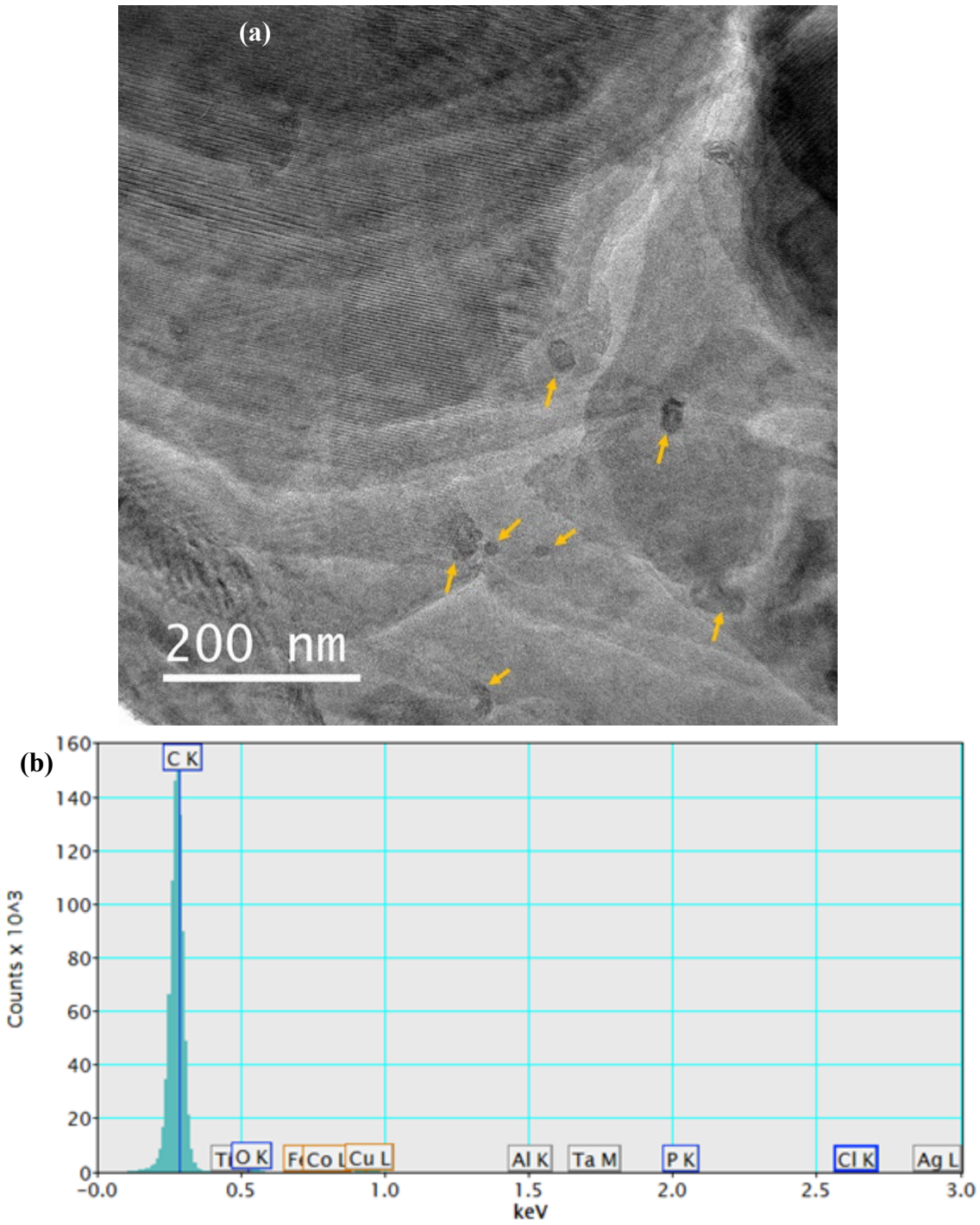

Fig. 4 The minicrystallites in as-received ImClO4: (a) a TEM image showing the tiny crystals indicated by gold arrows at 60,000 magnification, and (b) the corresponding XEDS spectrum acquired in *this region*

Another unique feature we found from the as-received $ImClO_4$ is the single crystalline morphology for even an extremely thin area. Figure 5 shows a more in-depth analysis for an extremely thin region inside the hole of the C support film

on the specimen with Fig. 5a showing the overview of this region of interest, and Fig. 5b exhibiting pronounced fringes as fine parallel straight lines. The inset in Fig. 5b is a fast Fourier transform diffraction corresponding to this high crystallinity. The blue bracket is the area within which a line profile across 28 fringes was measured for a 47.58-nm traveling distance. The periodic variation in their intensities is exhibited in Fig. 5c. The measured average spacing between each fringe is 1.70 nm, which we believe reflects the long-range order of crystallinity and is much larger than only one crystallographic diffraction plane; it most likely results from a specific domain and is related to the sample polarity. The high crystallinity for the as-received $ImClO_4$ is stable under the electron-beam exposure in TEM.

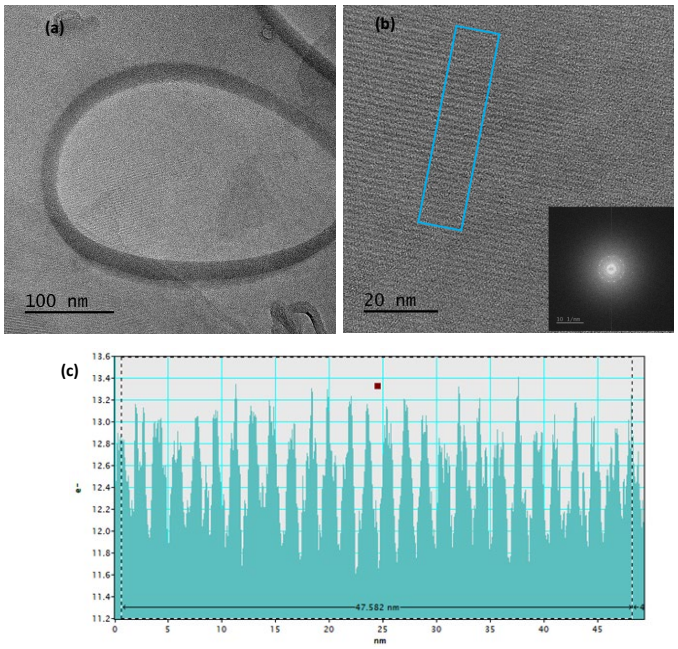

Fig. 5 Characterization of a thin region inside the hole of the carbon support film: (a) the crystalline morphology at 120,000 magnification, (b) an enlarged image taking at 500,000 magnification, and (c) the average line profile crossing 28 fringes acquired within the blue bracket enclosure in (b) with a measured total distance of 47.58 nm

Interestingly, after heating at 150 °C and subsequent cooling for DSC preparation, the depolarized $ImClO_4$ exhibits a dramatically different morphology from the as-received sample. As shown in Fig. 6, the sample appears to be a mixture of faceted crystals of several hundred nanometers size with thin sheets and flakes around and between the crystals. The majority of the material is still highly crystalline based on the strong contrast exhibited in the image. Detailed studies on the thin sheet region at high-resolution, as specified by the red bracket in Fig. 6a, revealed nanoscale short-range graphene-like morphology. On the other hand, the heated sample does not show any moiré fringes (Fig. 6b), suggesting the

disappearance of those crystalline domains found in the as-received sample (Fig. 5b). XEDS data for this region shows an increased O peak, while the Cl peak disappeared. Figure 6c shows the sheet/flake-like blanket with graphene-like short-range ordered structures.

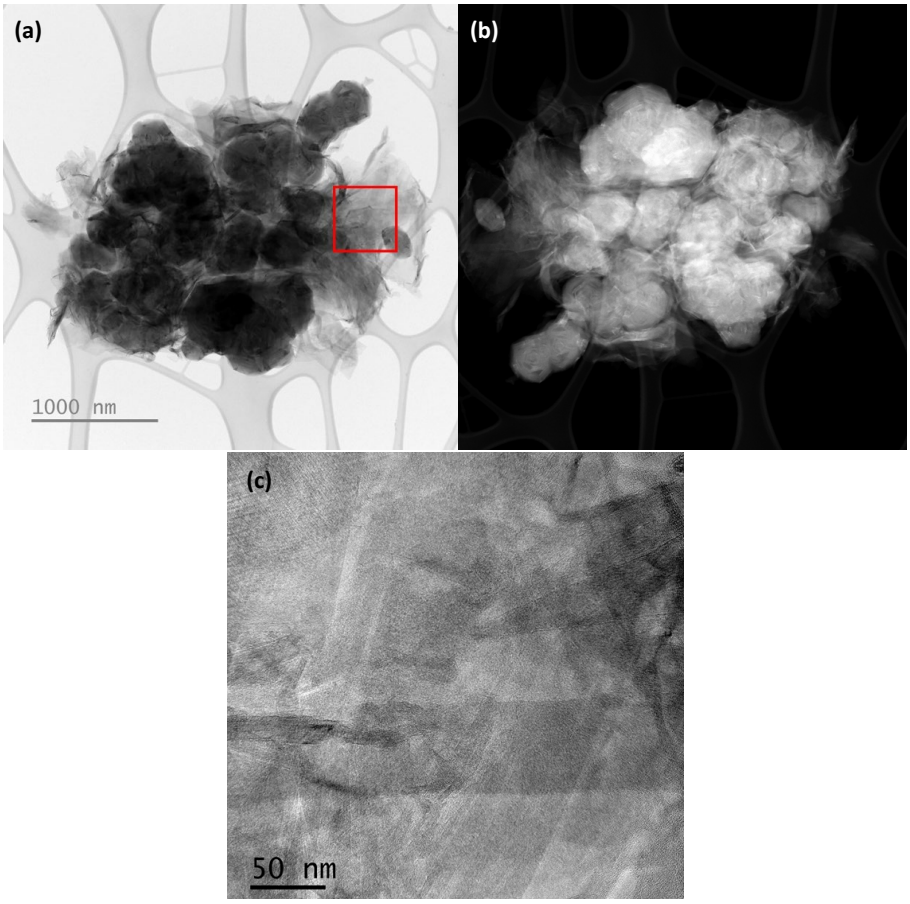

Fig. 6 TEM images of $ImClO_4$ after 150 °C heating: (a) a bright-field image showing a mixture of faceted crystals and thin sheets/flakes at 12,000 magnification, (b) a HAADF image of the same region in STEM mode, and c) the area of interest specified by the red bracket in (a) showing scattered short-range graphene-like morphology

Similar to the as-received $ImClO_4$, XEDS of the depolarized $ImClO_4$ still exhibits a tremendously large C peak overshadowing all other small peaks at full scale. After enlarging and overlaying the spectra to examine the changes of small peaks, the O peak increases while the Cl peak decreases after heating, as evidenced by the overlaying spectra shown in Fig. 7.

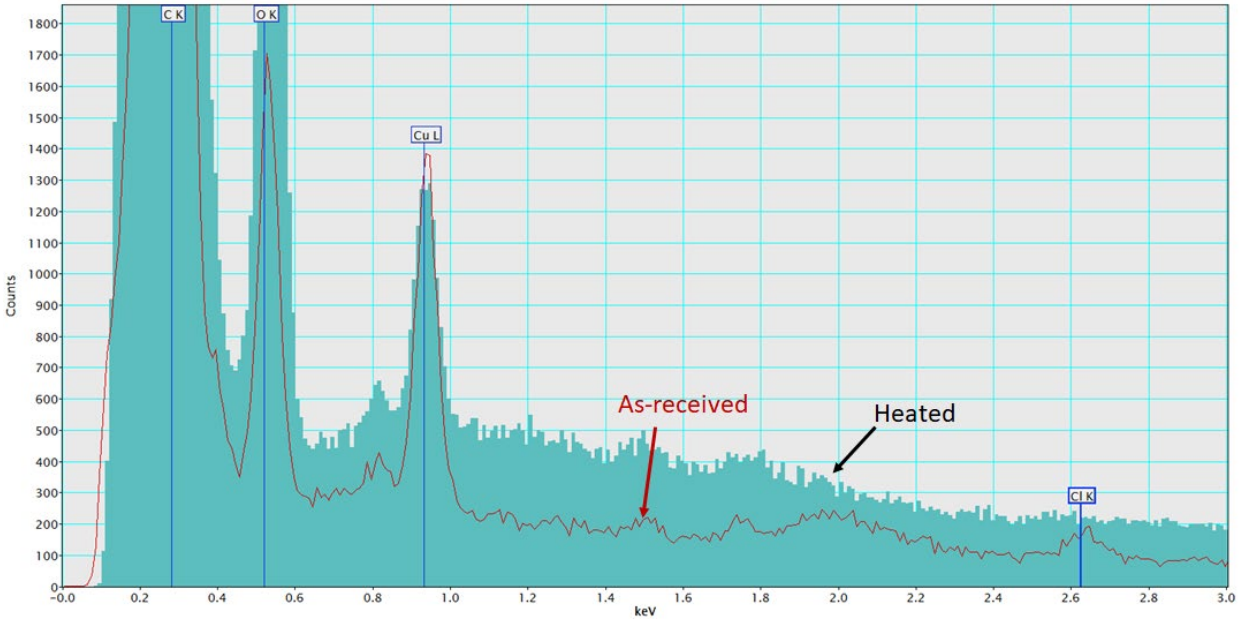

Fig. 7 Overlaid XEDS spectra of as-received and heated $ImClO_4$ samples showing the significantly increased O peak and decreased Cl peak

In contrast to the as-received sample, the thin areas of the heated $ImClO_4$ sample have disordered graphitic C morphology in TEM, and the structure continued to deteriorate quickly within several minutes when exposed to the electron beam in TEM. Figure 8 is a typical thin region showing the overview (Fig. 8a), and the significant graphitic C features from the regions enlarged and specified by the gold and red boxes in Fig. 8a are shown in Fig. 8b and 8c, respectively. Figure 9 is another thin area exhibiting onion-like graphene morphology.

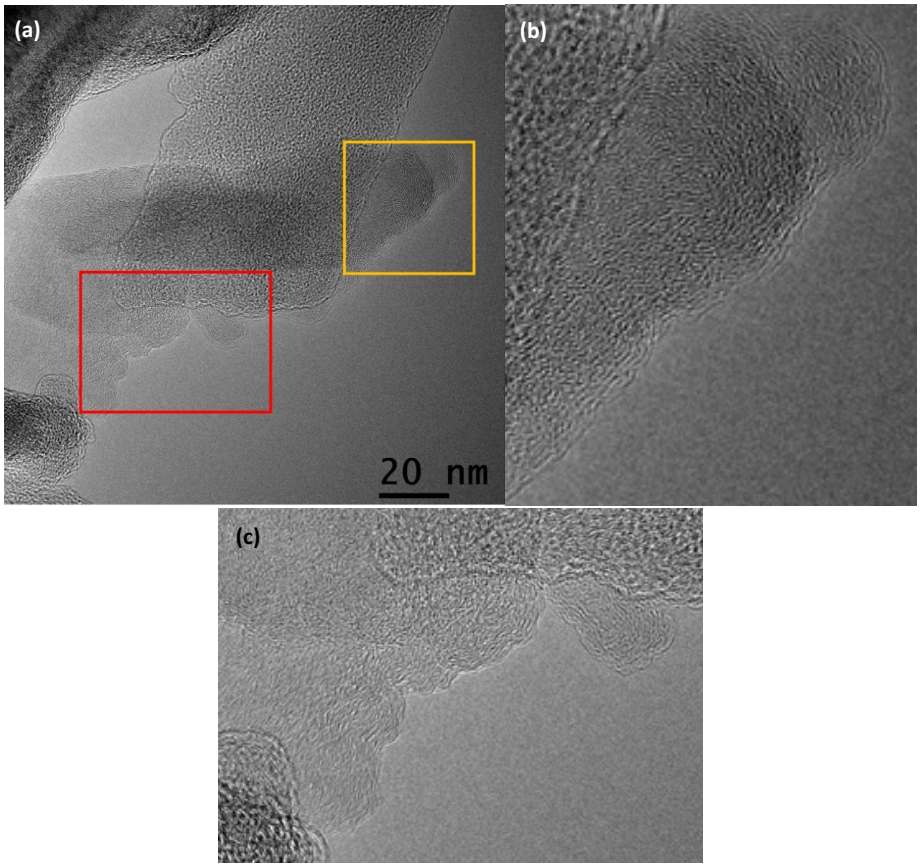

Fig. 8 TEM images of a thin region for the $ImClO_4$ after 150 °C heating showing (a) an overview at 300,000 magnification and enlarged views showing more details of the graphitic carbon morphology from regions specified (b) within the gold and (c) within the red bracket regions from (a)

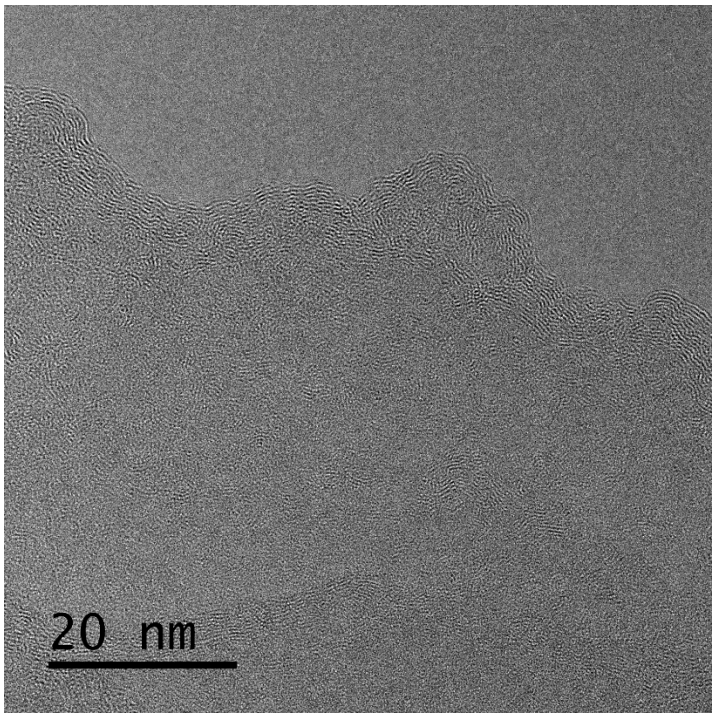

Fig. 9 TEM image showing long-range onion-like graphitic carbon morphology for the $ImClO_4$ after 150 °C heating

3.2 Thermo-Oxidative Behavior

DSC and TGA traces for as-received $ImClO_4$ are given in Fig. 10. The endotherms at 100 and 213 °C are associated with solid–solid phase transitions.[8] The 100 °C (373 K) transition (i.e., Curie point T_C) is more specifically associated with the second-order transition from the ferroelectric (I) to paraelectric (II) phase. The paraelectric mesophase II transitions to the high-temperature phase III at 213 °C (487 K). A large exotherm from the decomposition of $ImClO_4$ starts after approximately 320 °C, resulting in significant mass loss (IV). The decomposition enthalpy is 4424 J/g, comparable to that of HNS.[34] The small mass loss observed in the expanded-scale TGA trace shown in Fig. 10 (right) between 100 and 150 °C is not associated with a phase transition and is discussed in the context of D/P–GC/MS results.

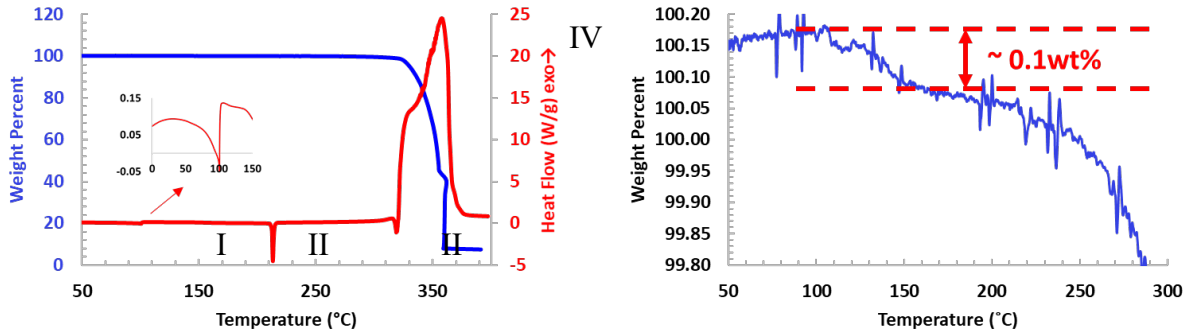

Fig. 10 (left) DSC and TGA results for as-received $ImClO_4$ obtained at a heating rate of 10 °C/min under N_2; insert gives expanded scale view of Curie point transition at 100 °C. (right) Expanded view of TGA at left shows mass loss between 100 and 150 °C. The loss is assumed to be due to volatilization of uncomplexed imidazole (as observed by D/P–GC/MS in Fig. 11).

D/P–GC/MS was performed to investigate the decomposition products, and the results are shown in Figs. 11 and 12. Under desorption conditions (Fig. 11), the as-received $ImClO_4$ was observed to desorb imidazole, which may be present in the sample as a result of incomplete reaction with perchloric acid during synthesis. Quick and Williams[6] found that imidazole rings can form complexes via H bonding to form imidazole imidazolium perchlorate. While this product is reported to be extremely sensitive to moisture and must be stored under special conditions to prevent decomposition, it is possible that it is present to a limited extent in our sample and that thermal treatment leads to loss of weakly bound imidazole rings, resulting in $ImClO_4$. We conclude that this process was responsible for the mass loss observed by TGA between 100 and 150 °C, and therefore constitutes on the order of 0.1 wt% of the as-received sample. The minicrystallites observed in the as-received sample (Fig. 4) may be related to the imidazole, since they do not contain O or Cl. When pyrolyzed at 350 °C (Fig. 12), an intense peak ranging 1.5–1.8 min was observed and found to be associated with several permanent gas combustion products (i.e., water [H_2O; m/z = 18], carbon monoxide [CO] and/or nitrogen [N_2] [m/z = 28], isocyanic acid [HNCO; m/z = 43], and carbon dioxide [CO_2; m/z = 44]). A much smaller peak associated with an unidentified imidazole-related species was also observed as a broad peak centered near 5.3 min. While hydrochloric acid (HCl) was not observed in the mass spectrum of the large peak between 1.5–1.8 min, it was observed in the peak for the unidentified imidazole, suggesting that the latter is associated with partially decomposed $ImClO_4$ (with the ring intact).

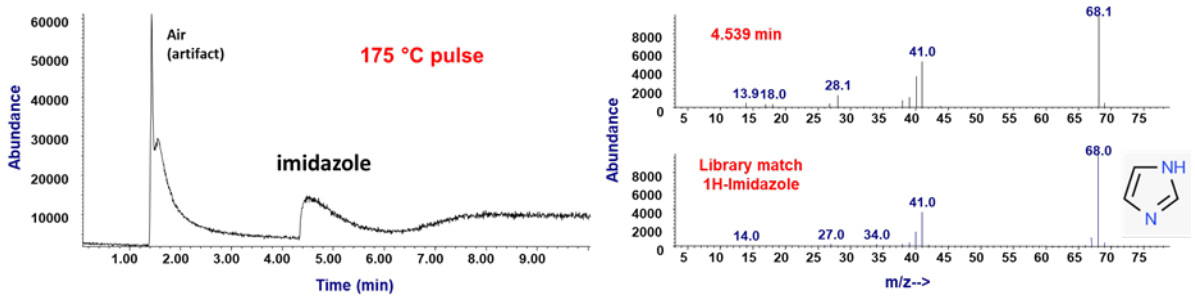

Fig. 11 D/P–GC/MS results for as-received $ImClO_4$ under desorption conditions (i.e., 175 °C interface and pulse). (left) Total ion chromatogram, and (right) mass spectrum of 4.5-min peak and library spectrum of 1H-imidazole.

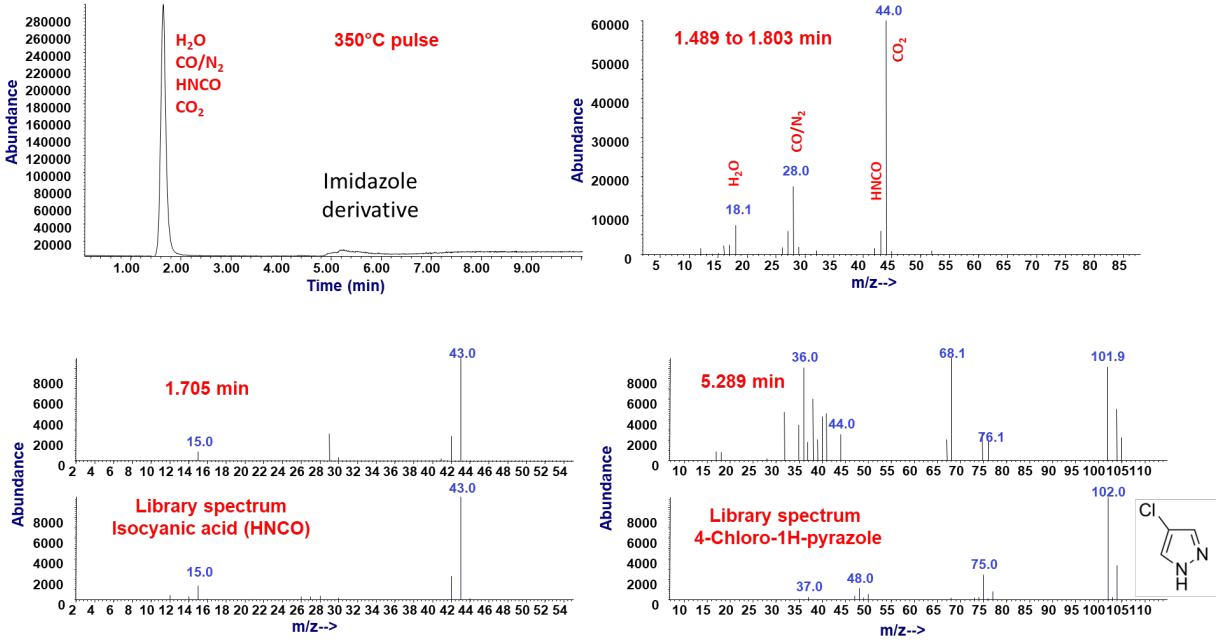

Fig. 12 D/P–GC/MS results for as-received $ImClO_4$ under pyrolysis conditions (i.e., 175 °C interface and 350 °C pulse). (top, left) Total ion chromatogram. (top, right) Mass spectrum of large peak ranging 1.5–1.8 min. (bottom, left) Mass spectrum of 1.7-min peak and library spectrum of HNCO. (bottom, right) Mass spectrum of 5.3-min peak and library spectrum of 4-chloro-1H-pyrazole. (Note 4-chloro-1H-pyrazole is not an exact match for the spectrum of the 5.3-min peak but suggests functional groups that might be present in the material giving rise to that peak. The obvious presence of HCl is indicated by m/z = 36.)

3.3 Influence of Polarization on Microsecond-Timescale Energy Release

3.3.1 Laser-Induced Shock Velocities

Figure 13 shows snapshots from the high-speed Schlieren video of the polarized and depolarized $ImClO_4$ following pulsed laser excitation during LASEM measurements. The expansion of the laser-induced shock wave into the air above the sample is used to quantify the microsecond-timescale energy release. While some variations in the hydrodynamic expansion of the laser-induced plasma plume are typically observed from shot to shot (i.e., variations in the shape of the expanding plasma plume), the visible emission from the laser-induced plasma is consistently slightly stronger and longer lasting for the depolarized sample, indicating some compositional differences.

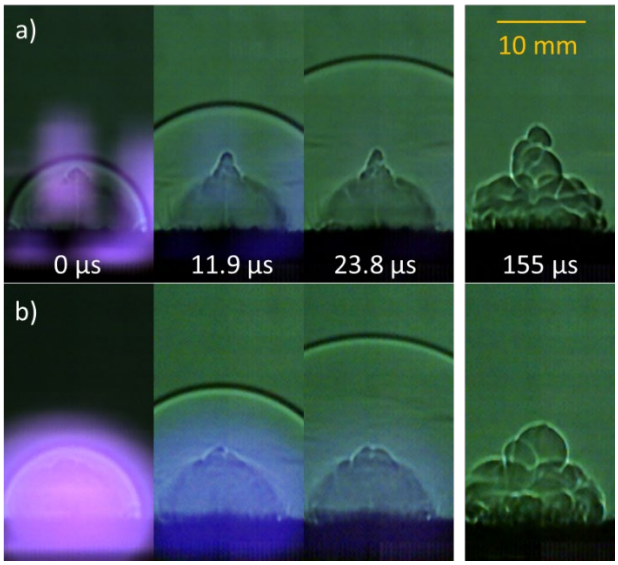

Fig. 13 Snapshots from the high-speed Schlieren video of laser-excited video of a) polarized and b) depolarized $ImClO_4$. Images have been cropped and the brightness increased by 40% for the last three frames of each series to better visualize the shock wave.

The characteristic laser-induced shock velocities for the polarized and depolarized $ImClO_4$ were measured for each laser shot based on a polynomial fit to the shock velocity versus time data. The averaged values and 95% confidence intervals are shown in Table 1. There is no statistical difference between the laser-induced shock velocities before or after heating of the sample to 150 °C. Using the previously determined calibration for this LASEM system,[33] the estimated detonation velocity for $ImClO_4$ was calculated based on the observed laser-induced shock velocity. These values (shown in Table 1) assume the material is detonable, that the high-temperature chemistry is similar to that of the conventional military explosives used

to determine the calibration, and that it can be pressed to the maximum theoretical density. The estimated detonation velocity for $ImClO_4$ is nearly identical to that of HNS (Fig. 14).

Table 1 Characteristic laser-induced shock velocities for polarized and depolarized $ImClO_4$

$ImClO_4$ (no. of shots)	Laser-induced shock velocity (m/s)	Estimated detonation velocity (km/s)
Polarized (25)	740.01 ± 11.14	7.20 ± 0.27
Depolarized (20)	738.33 ± 8.37	7.16 ± 0.21

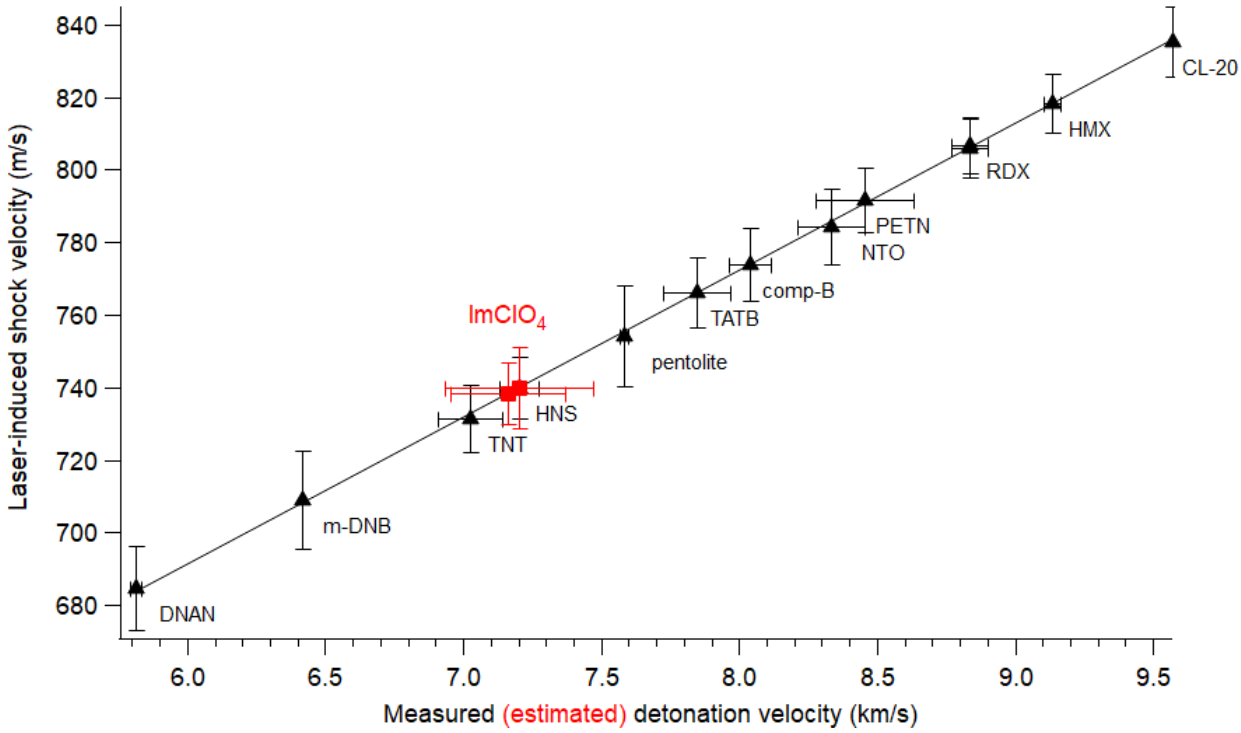

Fig. 14 Estimated detonation velocity for $ImClO_4$ compared with measured detonation velocities for conventional military explosives; $ImClO_4$ has the same laser-induced shock velocity as HNS[33]

3.3.2 Plasma Spectroscopy

During the passage of the laser-induced shock wave through the plasma region, the plasma emission was spectroscopically resolved and compared for the polarized and depolarized $ImClO_4$ (Fig. 15). In addition to the expected emission features from C, H, N, O, and Cl, we also see the formation of the cyano radical (CN) from molecular recombination reactions as the plasma cools and the presence of trace amounts of a calcium (Ca) impurity. Interestingly, while the intensity of most of

the emission features (including Cl) increased following depolarization of the sample, the C intensity decreased significantly—again suggesting a change in the material composition following heating.

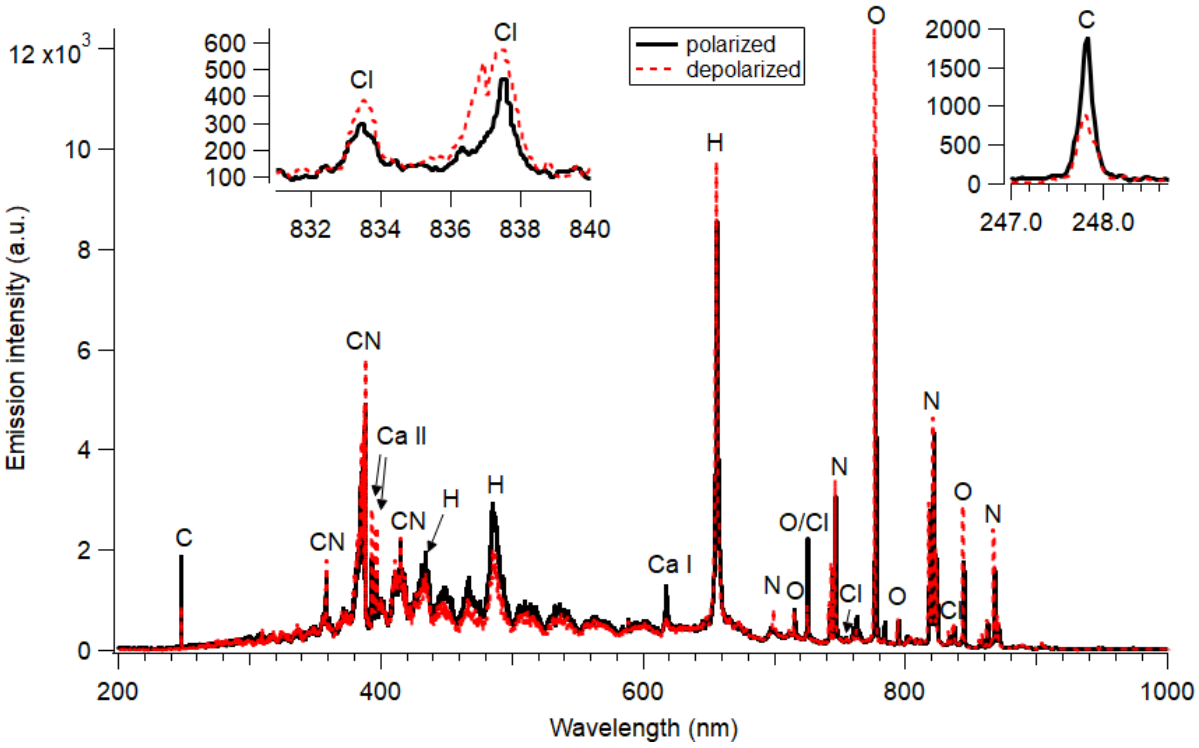

Fig. 15 Laser-induced plasma emission spectra for the polarized and depolarized $ImClO_4$ (averaged over 20 laser shots each)

The D/P–GC/MS results described in Section 3.2 explain the observed spectral differences (and visible emission differences in Fig. 13). Since the plasma emission spectra are generally sensitive down to the parts-per-million level for most species, the loss of 0.1-wt% imidazole during the thermal treatment to depolarize the crystals leads to a lower concentration of C (plus H and N) in the plasma. While the C line at 247 nm and H_β line at 486 nm decrease after depolarization, the H_α line at 656 nm and N lines increase. These increases are likely a result of changing plasma chemistry/temperature due to compositional differences and are affected by the entrainment of air into the laser-induced plasma (i.e., most of the O and N emission and some of the H emission originates from entrained air). The laser-induced shock velocities would not necessarily be influenced by the loss of 0.1-wt% imidazole unless there were some interaction between the $ImClO_4$ and the loosely bound imidazole that influenced the energy release[35] or damage to the remaining crystal,[36] as seen in previous studies. The striking morphology differences between the as-received (Fig. 3) and depolarized $ImClO_4$ (Fig. 6) do not appear to influence the microsecond-timescale energy release.

4. Conclusions

TEM images for the as-received $ImClO_4$ demonstrate highly crystalline morphology with strong contrast and pair-wise moiré fringes, presumably indicating crystal domains of various orientations. Carbonaceous minicrystallites with little or no O or Cl are also present in the images, suggesting they are related to the imidazole cation. While the as-received sample is highly stable to TEM beam exposure, the depolarized $ImClO_4$ exhibits amorphous flaky thin sheets with graphene-like morphology that rapidly decomposes in the electron beam. XEDS suggests that the O increases and Cl decreases following the thermal treatment. We postulate that fracturing of the large, heat-treated $ImClO_4$ crystals during TEM sample preparation led to perchlorate decomposition at the exposed surfaces, causing HCl to diffuse away and enabling oxidation of nearby carbon by O_2. It is also possible that thermal treatment of the sample to 150 °C led to some localized phase transformation of the $ImClO_4$ crystals, resulting in the observed morphological changes.

D/P–GC/MS showed that imidazole desorbs at low temperatures, which we believe is responsible for the 0.1-wt% mass loss between 100 and 150 °C and explains the decrease in C emission observed from the LASEM experiments. Decomposition at 350 °C leads to the formation of H_2O, CO and/or N_2, HNCO, CO_2, and an imidazole-related species associated with the loss of HCl. Despite the compositional and morphological changes associated with the thermal treatment to depolarize the $ImClO_4$ crystals, no differences in the microsecond-timescale energy release were observed. In addition, the estimated detonation velocity for $ImClO_4$ determined by LASEM (7.2 km/s) suggests that its detonation performance is equivalent to that of the military explosive HNS. Although the oxygen balance of $ImClO_4$ is not ideal for explosive ingredients, it could be suitable for specialized energetic applications due to its ferroelectric properties. Croconic acid is another ferroelectric material[37] that we have investigated as a potential energetic material that could find use in similar applications.[38–40]

5. References

1. Valasek J. Piezo-electric and allied phenomena in Rochelle salt. Phys Rev. 1921;17(4):475-481.
2. Lemaire E, Thuau D, Souetre M, Zgainski L, Royet A, Atli A. Revisiting two piezoelectric salts within an eco-design paradigm for sensors and actuators applications. Sens Actuator A-Phys. 2021;318:7.
3. Newnham RE, Eric Cross L. Ferroelectricity: the foundation of a field from form to function. MRS Bulletin 2005;30(11):845-848.
4. Nuraje N, Su K. Perovskite ferroelectric nanomaterials. Nanoscale. 2013;5(19):8752-8780.
5. Gao W, Chang L, Ma H, You L, Yin J, Liu J, Liu Z, Wang J, Yuan G. Flexible organic ferroelectric films with a large piezoelectric response. NPG Asia Mater. 2015;7(6):e189–e189.
6. Quick A, Williams DJ. The crystal structure of the complex salt imidazole imidazoloium perchlorate. Can J Chem. 1975;54.
7. Czapla Z, Dacko S, Kosturek B, Was'kowska A. Dielectric and optical properties related to phase transitions in an imidazolium perchlorate [C3N2H5ClO4] crystal. Physica Status Solidi (B). 2005;242(14):R122–R124.
8. Pająk Z, Czarnecki P, Szafrańska B, Małuszyńska H, Fojud Z. Ferroelectric ordering in imidazolium perchlorate. J Chem Phys. 2006;124(14):144502.
9. Przesławski J, Czapla Z. Calorimetric studies of phase transitions in imidazolium perchlorate crystal. J Phys Cond Matter. 2006;18(23):5517–5524.
10. Zhang Y, Liu Y, Ye H-Y, Fu D-W, Gao W, Ma H, Liu Z, Liu Y, Zhang W, Li J, Yuan G-L, Xiong R-G. A molecular ferroelectric thin film of imidazolium perchlorate that shows superior electromechanical coupling. Angew Chem Int Ed. 2014;53(20):5064–5068.
11. Ma H, Gao W, Wang J, Wu T, Yuan G, Liu J, Liu Z. Ferroelectric polarization switching dynamics and domain growth of triglycine sulfate and imidazolium perchlorate. Adv Electron Mater. 2016;2(6):1600038.
12. Hu Y, Guo Z, Ragonese A, Zhu T, Khuje S, Li C, Grossman JC, Zhou C, Nouh M, Ren S. A 3D-printed molecular ferroelectric metamaterial. PNAS. 2020;117(44):27204.

13. Hu Y, Liu Z, Wu C-C, Gottfried JL, Pesce-Rodriguez R, Walck SD, Chung PW, Ren S. Chemically driven energetic molecular ferroelectrics. Nature Comm. 2021; in press.

14. Badgujar DM, Talawar MB, Asthana SN, Mahulikar PP. Advances in science and technology of modern energetic materials: an overview. J Hazard Mater. 2008;151(2–3):289–305.

15. Yu Z, Bernstein ER. Experimental and theoretical studies of the decomposition of new imidazole based energetic materials: model systems. J Chem Phys. 2012;137(11):114303.

16. Yu Z, Bernstein ER. On the decomposition mechanisms of new imidazole-based energetic materials. J Phys Chem A. 2013;117(8):1756–1764.

17. Thomas E, Vijayalakshmi KP, George BK. Imidazolium based energetic ionic liquids for monopropellant applications: a theoretical study. RSC Adv. 2015;5(88):71896–71902.

18. Keshavarz MH, Pouretedal HR, Saberi E. A new method for predicting decomposition temperature of imidazolium-based energetic ionic liquids. ZAAC. 2017;643(2):171–179.

19. Hocaoğlu Ö, özbelge T, Pekel F, Özkar S. Aging of HTPB/AP-based composite solid propellants, depending on the NCO/OH and triol/diol ratios. J Appl Polym Sci. 2000;79(6):959–964.

20. Klapoetke TM, Sabate CM, Stierstorfer J. Hydrogen-bonding stabilization in energetic perchlorate salts: 5-Amino-1Htetrazolium Perchlorate and its adduct with 5-Amino-1H-tetrazole. Z Anorg Allg Chem. 2008;634:1867–1874.

21. Becker CR, Currano LJ, Churaman WA, Stoldt CR. Thermal analysis of the exothermic reaction between galvanic porous silicon and sodium perchlorate. ACS Applied Materials & Interfaces. 2010;2 (11):2998–3003.

22. Lewis WK, Harruff BA, Gord JR, Rosenberger AT, Sexton TM, Guliants EA, Bunker CE. Chemical dynamics of aluminum nanoparticles in ammonium nitrate and ammonium perchlorate matrices: enhanced reactivity of organically capped aluminum. J Phys Chem C. 2011;115(1):70–77.

23. Memon NK, McBain AW, Son SF. Graphene oxide/ammonium perchlorate composite material for use in solid propellants. J Propul Power. 2016;32(3):682–686.

24. Dai J, Wang F, Ru CB, Xu JB, Wang CG, Zhang W, Ye YH, Shen RQ. Ammonium perchlorate as an effective additive for enhancing the combustion

and propulsion performance of Al/CuO nanothermites. J Phys Chem C. 2018;122(18):10240–10247.

25. Zeng Z, Bernstein ER. Ammonium perchlorate and ammonium dihydrogen phosphate as energetic materials: comparison to ammonium nitrate. J Phys Chem C. 2019;123(19):12149–12153.

26. Cao W, Guo W, Ding T, Han Y, Li M, Gao D, Guo X. Laser ablation of aluminized RDX with added ammonium perchlorate or ammonium perchlorate/boron/magnesium hydride. Combust Flame. 2020;221:194–200.

27. Shin JH, Zhou M. Piezoelectric response of energetic composites under an electrostatic excitation. J Appl Phys. 2021;129(24):245103.

28. Saadon S, Sidek O. A review of vibration-based MEMS piezoelectric energy harvesters. Energy Conversion and Management. 2011;52(1):500–504.

29. Rossi C, Zhang K, Estève D, Alphonse P, Tailhades P, Vahlas C. Nanoenergetic materials for MEMS: a review. J Microelectromech Syst. 2007;16(4):919–931.

30. Row SL, Groven LJ. Smart energetics: sensitization of the aluminum-fluoropolymer reactive system. Adv Eng Mater. 2018;20(2).

31. Tarver CM. Effect of electric fields on the reaction rates in shock initiating and detonating solid explosives. AIP Conf Proc. 2012;1426(1):227–230.

32. Gottfried JL. Influence of exothermic chemical reactions on laser-induced shock waves. Phys Chem Chem Phys. 2014;16:21452–21466.

33. Gottfried JL. Laboratory-scale method for estimating explosive performance from laser-induced shock waves. Propellants Explos Pyrotech. 2015;40(5):674–681.

34. Silva Gd, Iha K, Cardoso AM, Mattos EC, Dutra RdCL. Study of the termal decomposition of 2,2',4,4',6,6'- hexanitrostilbene. J Aero Tech Manag. 2010;2(1):41–46.

35. Pesce-Rodriguez RA, Gottfried JL. Chemical analysis of amorphous nitramine energetic formulations. DEVCOM Army Research Laboratory (US); 2021 Apr. Report No.: ARL-TN-1055.

36. Gottfried JL, Pesce-Rodriguez RA, Farrow D, Dellinger J. Laboratory-scale investigation of the influence of ageing on the performance and sensitivity of an explosive containing e-CL-20. Propell Explos Pyrotech. 2018;43(6):616–625.

37. Horiuchi S, Tokunaga Y, Giovannetti G, Picozzi S, Itoh H, Shimano R, Kumai R, Tokura Y. Above-room-temperature ferroelectricity in a single-component molecular crystal. Nature. 2010;463(7282):789–792.

38. Jenkins TA, J.A.M. C-J, Gottfried JL, Pesce-Rodriguez RA, inventors. US Department of the Army, assignee. Energetic high pressure polymorph of croconic acid and high energy compositions formed therefrom. United States Patent US2017066706-A1; 2017 Dec 12.

39. Ciezak-Jenkins JA, Gottfried JL, Pesce-Rodriguez R. Thermal and laser-induced shock characterization of oxocarbon acids. Army Research Laboratory (US); 2014 May. Report No.: ARL-TR-6924.

40. Gottfried JL, Pesce-Rodriguez RA, Wu C-C. Validation of LASEM energy release predictions via detonation testing and analytical characterization. Army Research Laboratory (US); 2018 Oct. Report No.: ARL-TR-8557.

List of Symbols, Abbreviations, and Acronyms

3D	three-dimensional
ARL	Army Research Laboratory
C	carbon
Ca	calcium
Cl	chlorine
CO	carbon monoxide
CO_2	carbon dioxide
DEVCOM	US Combat Capabilities Developmental Command
D/P	desorption/pyrolysis
DSC	differential scanning calorimetry
FFT	fast Fourier transform
GC/MS	gas chromatography/mass spectrometry
H	hydrogen
H_2O	water
HAADF	high-angle annular dark-field
HCl	hydrochloric acid
HNCO	isocyanic acid
HNS	hexanitrostilbene
HRTEM	high-resolution bright field transmission electron microscopy
$ImClO_4$	imidazolium perchlorate
LASEM	laser-induced air shock from energetic materials
N	nitrogen
O	oxygen
PETN	pentaerythritol tetranitrate
STEM	scanning transmission electron microscopy

SUNY	State University of New York
T_C	Curie temperature or Curie point
TEM	transmission electron microscopy
TGA	thermogravimetric analysis
XEDS	X-ray energy dispersive spectra
UV	ultraviolet

1 (PDF)	DEFENSE TECHNICAL INFORMATION CTR DTIC OCA
1 (PDF)	DEVCOM ARL FCDD RLD DCI TECH LIB
12 (PDF)	DEVCOM ARL FCDD RLW WA J GOTTFRIED E WAINWRIGHT R PESCE-RODRIGUEZ E BYRD C-C WU K MCNESBY G SUTHERLAND D THAPA FCDD RLW WB J SABATINI B ROOS E JOHNSON FCDD RLW MC S WALCK
1 (PDF)	OSD OSD OUSD A-S P GUERIERI
1 (PDF)	BENNETT AEROSPACE, INC L GIRI
1 (PDF)	UNIVERSITY AT BUFFALO THE STATE UNIVERSITY OF NEW YORK–BUFFALO S REN
1 (PDF)	UNIVERSITY OF MARYLAND PETER CHUNG